

Analysis of real data acquired using the RGS

A. Rasmussen, J. Cottam, T. Decker, S. Kahn, M. Sako, J. Spodek, M. Stern
Columbia Astrophysics Laboratory, 538 West 120th Street
New York, NY 10027, United States of America

A. Brinkman, JW. den Herder, F. Paerels, C. de Vries, A. den Boggende
Space Research Organization of the Netherlands
Sorbonnelaan 2, 3584 CA Utrecht, The Netherlands

G. Branduardi-Raymont
Mullard Space Science Laboratory, Holbury St. Mary
Dorking, Surrey RH5 6NT, United Kingdom

C. Erd, G. Vacanti
European Space Research and Technology Centre (ESTEC), Space Science Department,
Astrophysics Division,
Postbus 299, NL-2200 AG Noordwijk, The Netherlands

H. Brauninger, W. Burkert
Max-Planck-Institut für extraterrestrische Physik, Testanlage PANTER,
Gautinger Str. 45, 82056 Neuried B. München, Germany

ABSTRACT

The RGS spectrometers aboard XMM offer new challenges in data analysis, since the instruments couple dispersive optics with complex angular redistribution functions (MM+RGA), with nondispersive, imaging spectrometer CCDs (RFC). While “modern” astrophysical, X-Ray spectral analysis incorporate extracted histograms and appropriate response matrices, the data parameter space available to the RGS for spectral extraction (and response matrix generation) includes a certain degree of freedom and a number of subtle, systematic effects. As an initial, exploratory analysis we reduce and extract multiple order spectra from several datasets acquired during ground calibration at the MPE-Panter testing facility. These are continuum source “observations” in which the entire RFC operates (9 CCDs simultaneously), reading out the nominal RGS band.

1. Introduction

In order to start analysing real data, some approximation to the behavior of the dispersive, reflection grating spectrometer must be made and consideration must be given to the nature of

the data delivered by the instrument. In the case of the RGS, a great deal of physical modelling and calibration have been done to understand the optical properties of the grating array and the charge transport properties of the focal plane CCDs¹. The present work is an attempt to bring characteristics of the individual RGS components together and model the response of the instrument sufficiently to compare with real data. In the following sections, a sample calculation of the point response function for the RGS is demonstrated, and how it is applied to formulate a response matrix. Effective area calculations for the RGS are also given, and finally, the response matrix is applied to some ground calibration datasets to outline one possible method for analysing RGS data.

2. RGS point response functions and response matrices

The general point response function (PRF) of the RGS is a multidimensional probability distribution function that connects physical photon properties (2–dimensional off–axis angle and wavelength) to detector coordinates (spatial pixel number and CCD pulseheight value). Cast as a distribution in the 3 measurable quantities, the CCD pulseheight (ph), the dispersion angle (β) and the cross dispersion position (y), an approximate expression would be:

$$\text{prf}_{\text{gen}}(ph, \beta, y|\lambda, \phi, \psi) = g\left(\beta|\lambda, \alpha_0 + \frac{F}{L}\phi\right) p(ph|\lambda) c(y|\beta, \phi, \psi) v(\beta) A_{\text{eff}}^g(\lambda|\phi, \psi) \quad (1)$$

where λ is the wavelength of the light and ϕ and ψ are off–axis angles of the source in the dispersion direction and cross dispersion direction, respectively. Other variables and constants employed in this expression are the nominal angle of incidence to the gratings α_0 , and the telescope focal length and grating distance F and L , respectively. $g()$ is the angular redistribution function and reflectivity of the gratings, $p()$ the CCD’s efficiency and pulseheight response function, $c()$ is the cross–dispersion distribution function of the spectrometer, $v()$ is the vignetting function of the grating array and $A_{\text{eff}}^g()$ is the effective area of the telescope as it illuminates grating replica faces.

For simplified analysis purposes however, we consider PRFs of reduced dimensionality: as functions of the dispersion variable, after having integrated prf_{gen} over its other detector coordinates (cross dispersion and the CCD’s pulseheight). The detailed shape of the reduced PRFs are thus *functionals* of the actual extraction window through which 1) data is extracted, and 2) the general PRF is integrated.

In order to calculate the reduced PRF then, a minimum of three ingredients are required: 1) the monochromatic angular redistribution of the grating array, 2) the monochromatic pulse redistribution function of the CCDs, and 3) the extraction window defined in the dispersion–pulseheight detector coordinate plane. For the time being we neglect windowing in the cross

¹in particular, look for contributions by J. Cottam, F. Paerels, C. de Vries and J. Spodek in this volume.

dispersion direction and chip-to-chip CCD electronic and quantum efficiency differences. The reduced PRF may be expressed in terms of prf_{gen} :

$$\text{prf}_{\text{red}}(\beta|\lambda) = \int d(\text{ph}) b(\beta, \text{ph}) \text{prf}_{\text{gen}}(\text{ph}, \beta|\lambda), \quad (2)$$

where $b()$ is the region definition or “window” defined in the $\beta - \text{ph}$ plane, which evaluates to 1 within the region and 0 elsewhere.

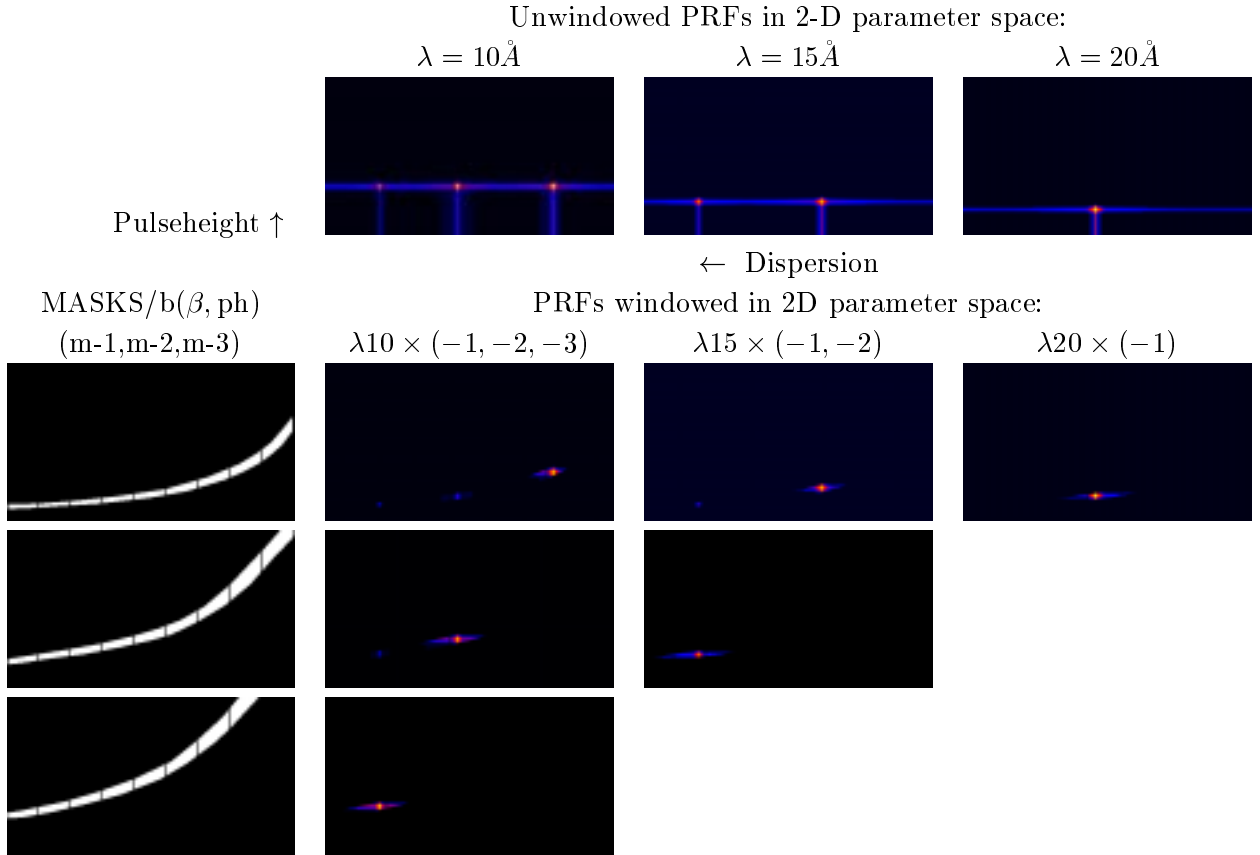


Fig. 1.— Figures demonstrating the 2-D windowing of the 2-D PRFs for three monochromatic distributions. The top row of false color plots give the unwindowed response distributions in dispersion (horizontal axis) and CCD pulseheight (vertical axis), while subsequent rows give windowed distributions preceded by the mask applied in each case, for $m=1, -2$ and -3 , respectively. The same distributions, collapsed in the dispersion coordinate and in pulseheight, are given the lower left and lower right plots respectively, of Fig 2.

Examples of monochromatic PRFs, displayed in the $\text{ph} - \beta$ plane, are shown in the top row of Fig. 1. This unwindowed, 2-D PRF is separable, equal to the product of a function in β and

a function in ph (examples of each shown in the top plots of Fig. 2). The windowing meanwhile, alters the distributions as shown in the bottom two plots: it reduces the response away from “nominal” parameter volume contained in the extraction window. When the extraction window is used to filter individual events, it effectively reduces the distribution of events falling far from the response feature that is largely contained in the extraction window.

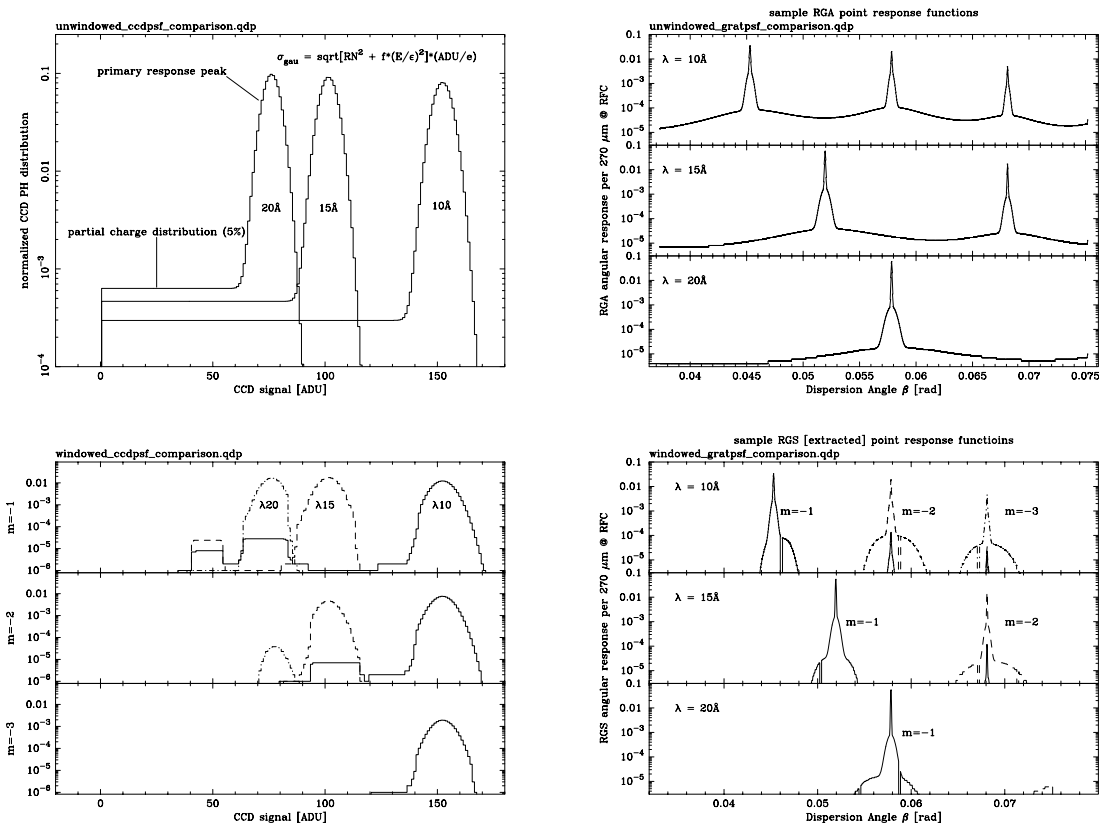


Fig. 2.— Examples of reduced PRF calculations for unwinded (top row) and windowed (bottom row) CCD pulseheight distributions (left column) and grating dispersed angular distributions (right column) for 10, 15 and 20Å light into the XMM telescope. The windowing effectively reduces “nondiagonal” elements in the response matrix, as demonstrated in Fig. 3. These 1-D distributions are also displayed in 2-D representation in Fig. 1.

The response matrix for the instrument then, is an array of point response functions appropriate for the extraction volume in question. Figure 3 is an example of such a matrix: the top density map represents the response matrix for no windowing, while the bottom represents windowing of the response through a nominal $m = -1$ extraction region, or banana.

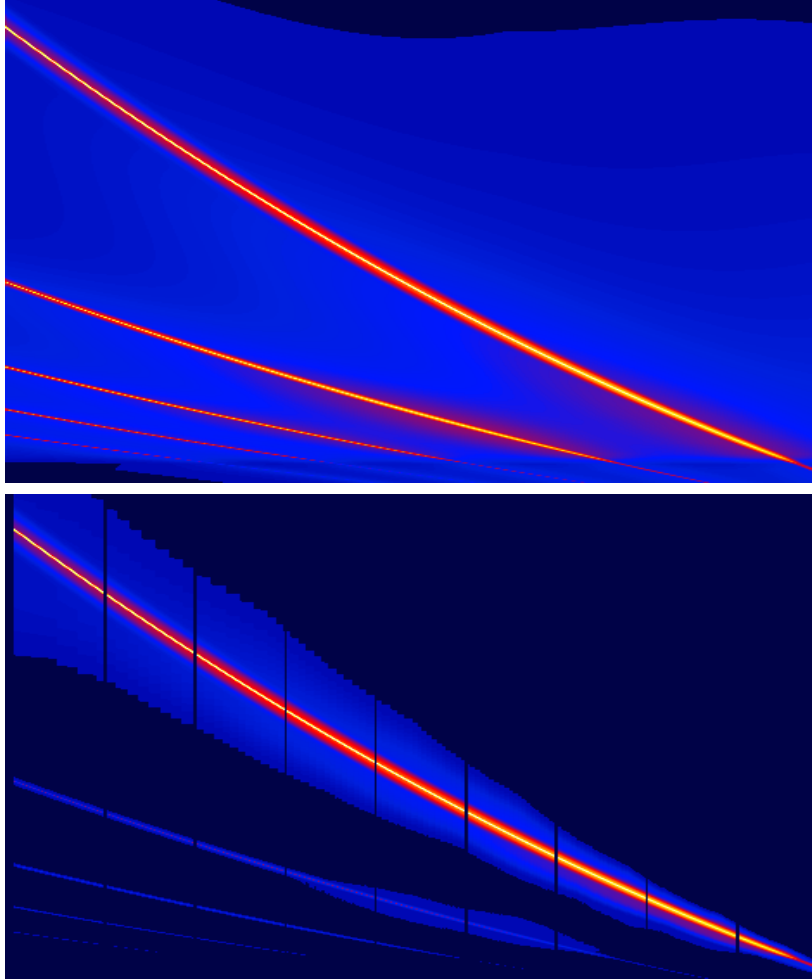


Fig. 3.— “Banana space” windowing effects to the RGS response matrix. The horizontal axis in both plots represents the spectrometer’s dispersion axis, in which β increases toward the left (longer wavelength), while the vertical axis represents the wavelength scale with a suppressed zero. Top: a graphical representation of an unwindowed response matrix. In this plot, each line represents an angular probability distribution, encoded in false color and logarithmic scale. Bottom: the same response matrix, but with the PRF windowed through the nominal, $m=-1$ “banana” mask (see appropriate plot in Fig. 1). This windowed, largely diagonalized response matrix is appropriate for analysing data extracted using the same, $m=-1$ “banana” mask. Gaps between chips in the RFC are included in this mask.

3. RGS effective areas

The effective area of the RGS system naturally depends on the extraction region, and thus any estimate for $A_{\text{eff}}^{\text{rgs}}(\lambda)$ is accompanied by its extraction region $b(\cdot)$:

$$A_{\text{eff}}^{\text{rgs}}(\lambda) = \int d\beta \text{prf}_{\text{red}}(\beta|\lambda) = \int d\beta \int d(\text{ph}) b(\beta, \text{ph}) \text{prf}_{\text{gen}}(\text{ph}, \beta|\lambda). \quad (3)$$

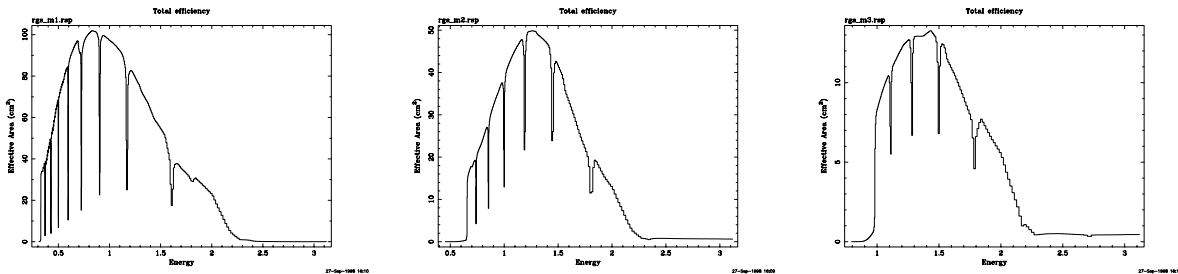


Fig. 4.— Effective area calculations, extracted using the $m = -1$, -2 and -3 “banana” windows displayed on the left of Fig. 1, respectively. The $m = -1$ effective area curve is equivalent to a collapse (over β) of the lower response matrix in Fig. 3

Figure 4 shows sample single telescope, effective area curves, based on current estimates, and the three different extraction regions (“bananas”) shown in Fig. 1. No cuts in the cross-dispersion direction were performed and no attempts have been made to compare these curves with other effective area measurement results² The grating’s dispersion distribution used was the current, best model,³ but the CCD pulseheight redistribution function used is a simplistic, Gaussian primary response feature (Fano + $5 e^-$ readout noise) plus a 5%, partial charge tail extending uniformly from 0 up to the center of the primary feature (shown in the upper left plot of Fig. 2). Such a simple approximation is subject to improvement but useful for the time being because it qualitatively reproduces some of the real response features seen in the data.

4. Windowing the data in parameter space

The key idea behind this work is that the same region $b(\beta, \text{ph})$ must be used to extract the data as was used to fashion the response function. The data presented below was acquired on 18 different CCD readouts (on 9 different chips), and some nominal corrections were applied (offset, gain, CTIs and event reconstruction) to the data from individual readouts so that a common

²see contribution by C. de Vries in this volume.

³cf. <http://astro1.nevis.columbia.edu/xmm/documents/cal98023> by Jean Cottam.

pulseheight grid is populated with the data. That common grid necessarily matches the CCD gain assumed in Eq. 2, the calculation for $\text{prf}_{\text{red}}()$. With the data thus “homogenized”, the windowing of the data is straightforward and yields multiple order spectra as shown in Fig. 5.

5. Extracted spectra, response matrices and analysis codes

At least two codes (XSPEC and SPEX) for spectral analysis are in common use by X-Ray astronomy community. In addition to extracted histograms (or pulseheight files), both brands of code require response matrices, or some abbreviated simulator of the instrument that is appropriate for the dataset in question. Here we very briefly “analyse” the extracted spectra (*e.g.*, those shown in Fig. 5) with the help of response matrices generated using the same extraction parameters. Figures 6, 7 and 8 display multiple order extractions for continuum observations of Au, Macor and $\text{SiO}_2 + \text{Co}(1\mu\text{m})$, respectively. Each individual spectral extraction (and model) includes an abundance of information, which is hardly touched upon here, perhaps slightly in the figure captions. In each case, a single emission model (constrained by the $m = -1$ spectrum) is applied to 2 or 3 extractions (always using response matrices appropriate for the extraction in question). In general, even with this very preliminary treatment of the RGS’s characteristics, the energies of individual spectral features agree well (within about 1 eV) of tabulated laboratory values, and the match between data and model for the continuum levels in $m = -2$ is reasonably good (simultaneously with the $m = -1$ fit).

6. Conclusion

While the $m = -1$ and -2 extractions appear quantitatively consistent with their respective response matrices (both in terms of their wavelength solutions and effective area functions), the $m = -3$ matrix contains too much response, which was a known problem. Also, although it was not presented above, there is evidence that the angular redistribution function $g()$ requires additional understanding in its dependence on energy. The self-consistent, histogram extraction and response generation described above has proven to be a useful method by which such problems can be identified and quantified. Whether such procedures can be implemented into routine, XMM “pipeline data products” obviously depends upon the stability of instrumental parameters, efficient and practical aspect correction and the appropriate response exposure mapping procedures executed in parallel. These issues are currently under investigation. In any case, the 2-dimensional view (banana plot) of the multi-order, entire RGS spectrum proves to be an indispensable utility in understanding the nature of features in individual extracted spectra.

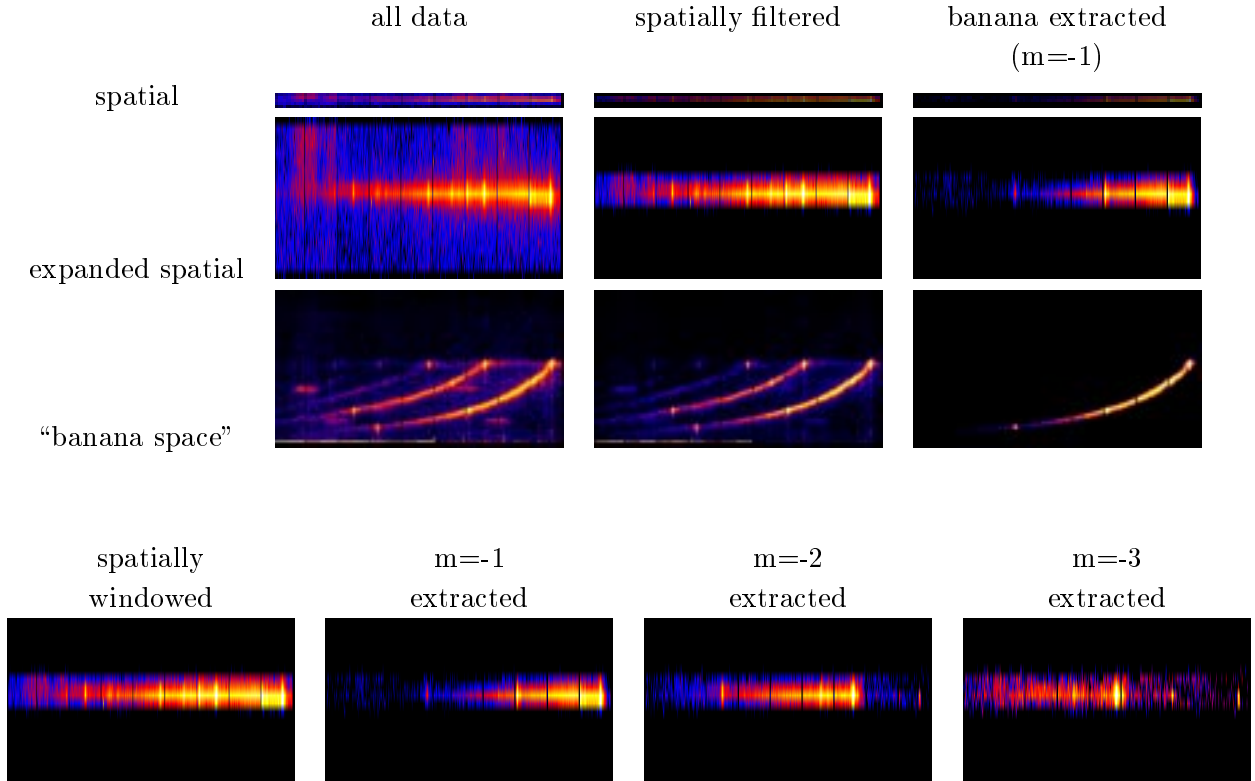


Fig. 5.— Progressive windowing of the homogenized CCD data. The upper plot group shows, for three stages of the windowing, the spatial event distribution (top), an expanded scale of the same map (middle) and the dispersion–pulseheight (“banana space”) event distribution. The left group of plots show the distribution of events after hot/flickering pixel and cosmic ray removal. The center group is the distribution after spatial filtering (a narrow aperture in the cross dispersion direction), and the right group shows the distribution after windowing through the $m = -1$ extraction region shown in Fig. 1. Events due in-flight calibration radioactive sources in the RFC are seen clearly in the leftmost banana plot and are strongly rejected in the corresponding center plot. The bottom row of images show spatial distributions for banana extracted spectra for the $m = -1$, -2 and -3 regions, preceded by the map containing all orders. Two of these extractions are displayed in histogram form in Fig. 6.

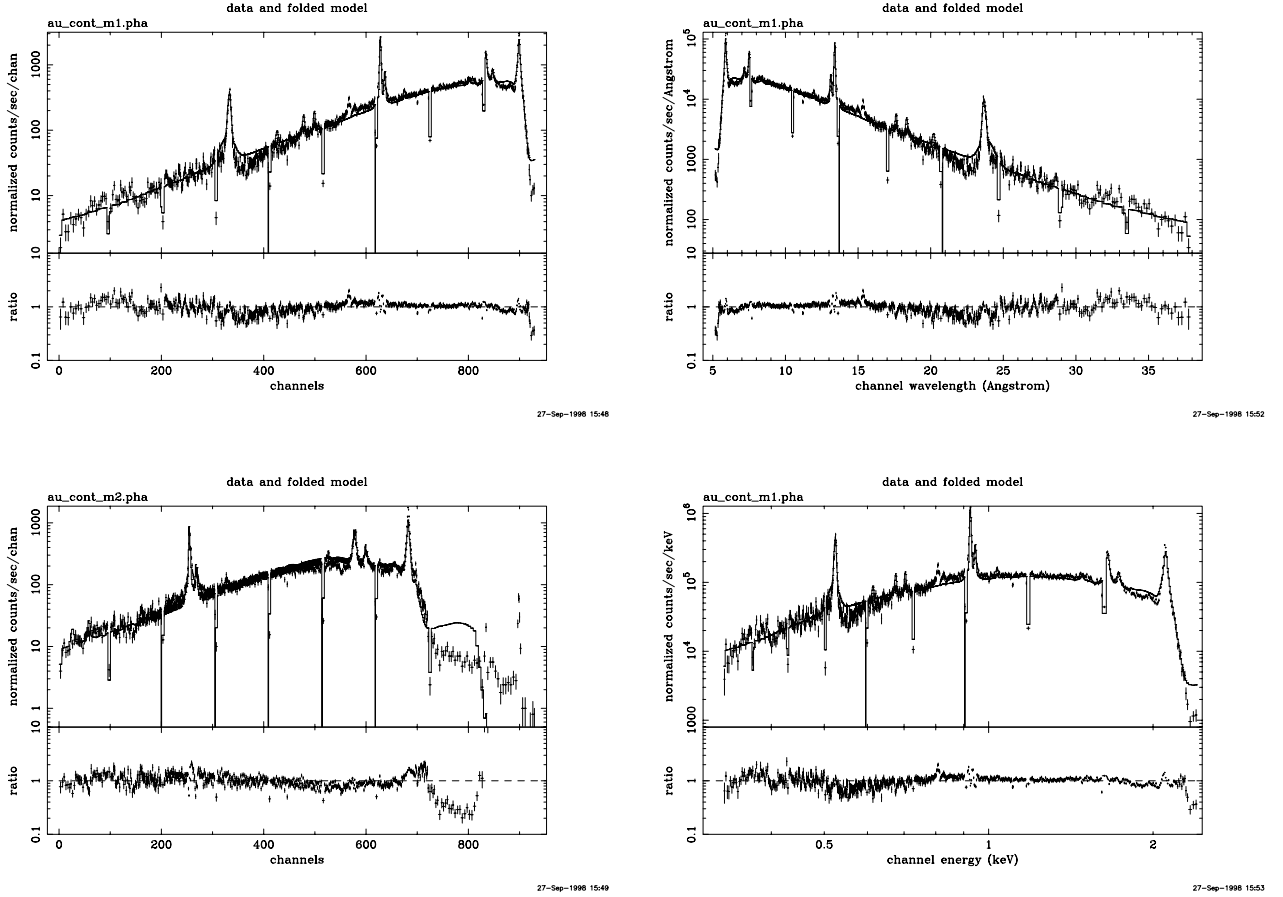


Fig. 6.— MPE–Panter Au target source continuum exposure. Two of the extracted spectra from Fig. 5 ($m = -1$ and -2) are shown here and modelled using XSPEC and the response matrices generated as described above (the $m = -1$ matrix is shown in Fig. 3). Because the emission characteristics of the source are not easily calculable, an heuristic model was applied (powerlaw + broad lines) and fit to the $m = -1$ upper left histogram. The same model was transferred to the $m = -2$ histogram (and its corresponding matrix). Each histogram is accompanied by a “ratio” plot which displays the ratio of the residuals (data - model) to the model. The plots on the right display the $m = -1$ data arranged by channel wavelength and channel energy, which are values included in the response matrix.

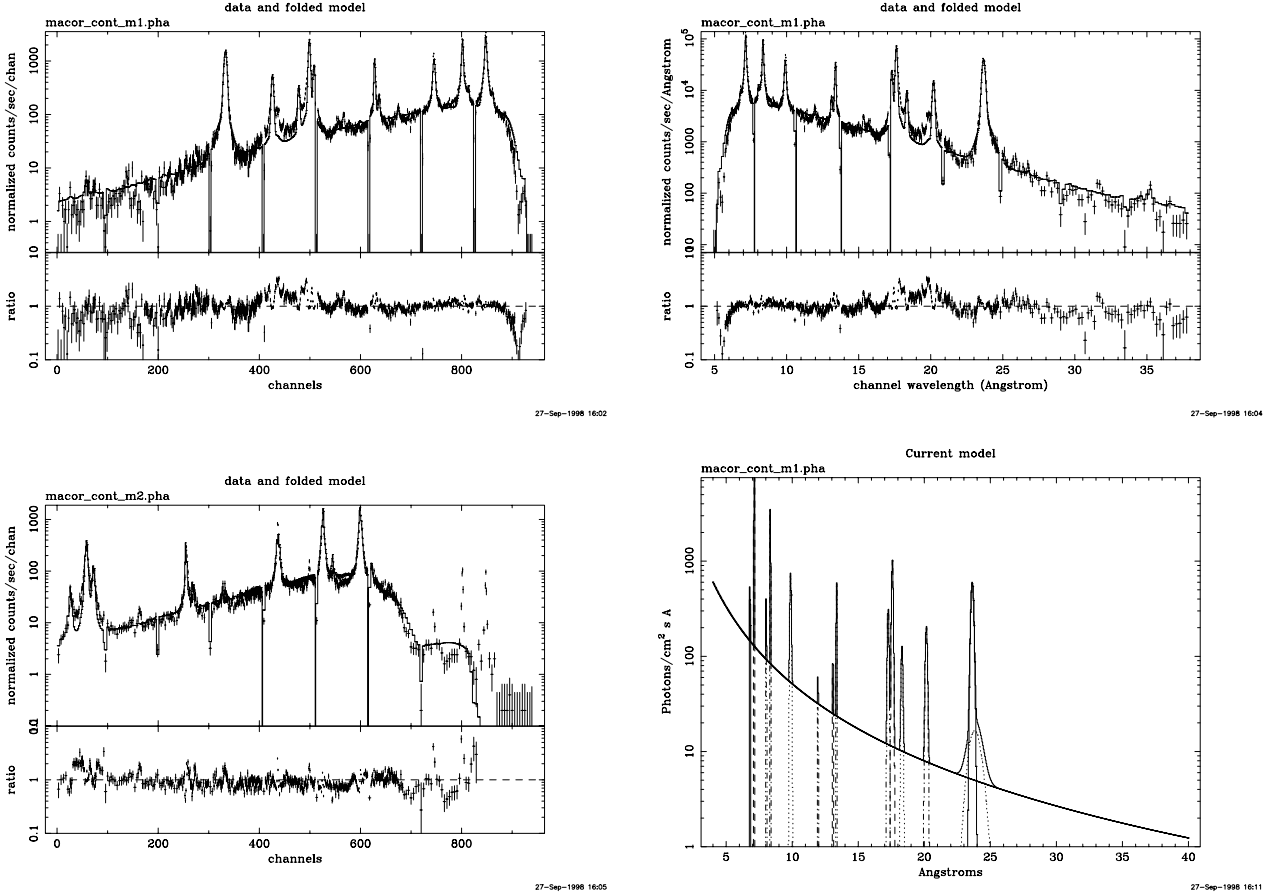


Fig. 7.— MPE-Panter Macor (machinable porcelain) target source continuum exposure. As in Fig. 6, an heuristic model was applied to the $m = -1$ histogram and transferred to the $m = -2$ dataset. Macor contains an abundance of the lighter elements in the periodic table, and the features identified include line complexes of Si K, Mg K, Al K, Cu L, Fe L, F K and O K, although some features remain unidentified or unmodelled. Nearly all of the features match within 1 eV of tabulated X-Ray emission line energies. Complex edgelike features in the continuum above 1.84 keV are most definitely extended X-Ray absorption fine structure (EXAFS) in the Silicon of the Macor. The sharp emission features seen in the $m = -2$ plot, absent in the emission model are event pileup effects that are coincident in location to sharp features in the $m = -1$ data.

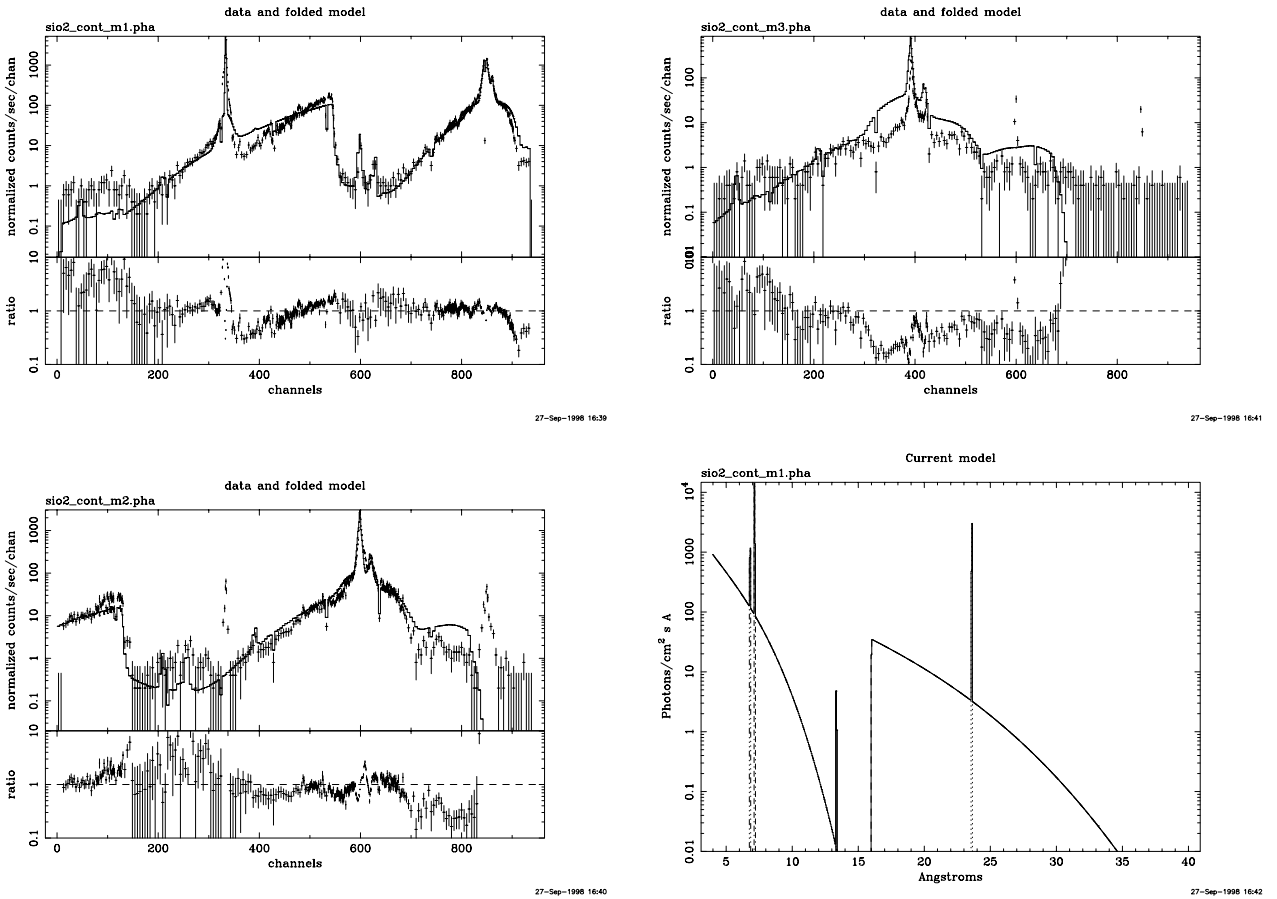


Fig. 8.— MPE–Panter SiO₂ target source continuum exposure, with a 1 μm Cobalt filter imposing a strong Co L_{III} edge in the continuum, in the middle of the nominal RGS $m = -1$ band. These plots show the $m = -1$, -2 and -3 spectral extractions of the dataset, along with a (usual) heuristic model. The depth of the edge is strong: the events located where the absorption is large are redistributed from other regions of the emission spectrum. The $m = -3$ dataset is modelled poorly, due to a known overestimation of the grating efficiency in that order. The two features in the saddle of the absorption edge are interesting because one is part of the prf_{red} for the bright, Si K emission feature while the other is a true emission line corresponding to Cu L. As usual, the simple model used does not attempt to fit the real O K absorption feature, nor the Si K EXAFS features which are also seen here.

REFERENCES

- Brinkman, A. C. *et al.*, "The reflection grating spectrometer on-board XMM", in EUV, X-Ray, Gamma-Ray Instrumentation for Astronomy VIII, O. Siegmund and M. Gummin, eds., Proc. *SPIE* **2808**, pp. 463-480, 1996.
- Cottam, J., "New model of the RGS grating efficiency",
<http://astro1.nevis.columbia.edu/xmm/documents/cal198023.ps>, 1998.
- Cottam, J., "Preliminary model of the RGS grating efficiency",
<http://astro1.nevis.columbia.edu/xmm/documents/cal197001.ps>, 1997.
- Cottam, J., "How to use the RAW-EFFICIENCY.TABLE file",
<http://astro1.nevis.columbia.edu/xmm/documents/cal197003.ps>, 1997.
- Kahn, S. *et al.*, "The reflection grating arrays for the reflection grating spectrometer on-board XMM", in EUV, X-Ray, Gamma-Ray Instrumentation for Astronomy VIII, O. Siegmund and M. Gummin, eds., Proc. *SPIE* **2808**, pp. 450-462, 1996.
- Paerels, F., "Short summary of the preliminary assessment of the scientific performance of RGA/FM2", <http://astro1.nevis.columbia.edu/xmm/documents/cal198014.ps>, 1998.
- Paerels, F., "Repositioning the RGA and RFC on FM1",
<http://astro1.nevis.columbia.edu/xmm/documents/cal198005.ps>, 1998.
- Paerels, F., "Effect of the RGA Braces on EPIC and RGS Performance",
<http://astro1.nevis.columbia.edu/xmm/documents/mod97002.ps>, 1997.
- Rasmussen, A. *et al.*, "Component level summary for the contents of grating arrays RGA1 and RGA2", <http://astro1.nevis.columbia.edu/xmm/documents/cal198009.ps>, 1998.
- Rasmussen, A. *et al.*, "Performance characterization of the reflection grating arrays (RGA) for the RGS experiment aboard XMM", in X-Ray Optics, Instruments, and Missions, R. B. Hoover and A. B. C. Walker II, eds., Proc. *SPIE* **3444**, 1998, in press.
- Spodek, J., "Preliminary analysis of the (RGA) FM2 point spread function data",
<http://astro1.nevis.columbia.edu/xmm/documents/cal198006.ps>, 1998.
- Spodek, J., "Measurement of single grating scatter at the Nevis longbeam facility",
<http://astro1.nevis.columbia.edu/xmm/documents/cal197002.ps>, 1997.
- Spodek, J., "Reanalysis of Panter (RGA) FM1 LSF data",
<http://astro1.nevis.columbia.edu/xmm/documents/cal197018.ps>, 1997.
- Spodek, J., "Further analysis of Panter (RGA) FM1 LSF data",
<http://astro1.nevis.columbia.edu/xmm/documents/cal197024.ps>, 1997.

